



Optics Letters

105° field of view non-contact handheld swept-source optical coherence tomography

SHUIBIN NI,¹ THANH-TIN P. NGUYEN,¹ RINGO NG,² SHANJIDA KHAN,^{1,3} SUSAN OSTMO,¹ YALI JIA,^{1,3} MICHAEL F. CHIANG,⁴ DAVID HUANG,^{1,3} J. PETER CAMPBELL,¹ AND YIFAN JIAN^{1,3,*}

¹ Casey Eye Institute, Oregon Health & Science University, Portland, Oregon 97239, USA

² School of Engineering Science, Simon Fraser University, Burnaby, British Columbia V5A 1S6, Canada

³ Department of Biomedical Engineering, Oregon Health & Science University, Portland, Oregon 97239, USA

⁴ National Eye Institute, National Institutes of Health, Bethesda, Maryland 20892, USA

*Corresponding author: jian@ohsu.edu

Received 20 September 2021; revised 14 October 2021; accepted 3 November 2021; posted 8 November 2021 (Doc. ID 443672); published 22 November 2021

We demonstrate a handheld swept-source optical coherence tomography (OCT) system with a 400 kHz vertical-cavity surface-emitting laser (VCSEL) light source, a non-contact approach, and an unprecedented single shot 105° field of view (FOV). We also implemented a spiral scanning pattern allowing real-time visualization with improved scanning efficiency. To the best of our knowledge, this is the widest FOV achieved in a portable non-contact OCT retinal imaging system to date. Improvements to the FOV may aid the evaluation of retinal diseases such as retinopathy of prematurity, where important vitreoretinal changes often occur in the peripheral retina. © 2021 Optica Publishing Group under the terms of the Optica Open Access Publishing Agreement

<https://doi.org/10.1364/OL.443672>

Ultra-wide-field (UWF) optical coherence tomography (OCT) imaging technology has the potential to improve the detection and management of many diseases involving the peripheral retina. This includes retinopathy of prematurity (ROP), one of the leading causes of blindness and vision impairment in children [1], where adequate visualization of the peripheral retina is important for diagnosis and staging. While it is possible to achieve a larger field of view (FOV) by montaging smaller images together, this requires more time and complex imaging processing, and may limit the ability of future algorithms to do automated segmentation of retinal structures and biomarkers. An expanded FOV allows the clinician to obtain more complete, continuous imaging of posterior and peripheral retinal pathology in a single capture. In the past, it has proven challenging to design a high-speed, wider FOV OCT system in a portable format owing to the weight and size constraints of the probe. Several experimental prototype handheld OCT systems were developed for various clinical applications over the past decade; however, there are no portable OCT systems that can acquire images from the posterior pole to peripheral retina in a single, non-contact capture. We summarized the A-line rate and FOV of existing handheld OCT systems designed for retinal imaging

Table 1. Comparison of Published Handheld OCT System, Designed for Retinal Imaging, Listed by the Date of Publication

Previous Publications	A-line Rate	Field of View
Woonggyu Jung, <i>et al.</i> [2]	140 kHz	10°
Chen D. Lu, <i>et al.</i> [3]	350 kHz	43°
Derek Nankivil, <i>et al.</i> [4]	100 kHz	22°
Francesco Larocca, <i>et al.</i> [5]	20 kHz	8.8°
Jianlong Yang, <i>et al.</i> [6]	100 kHz	40°
J. Peter Campbell, <i>et al.</i> [7]	100 kHz	100°
Oleg Nadiarnykh, <i>et al.</i> [8]	350 kHz	28°
Shaozhen Song, <i>et al.</i> [9]	200 kHz	72°
Christian Viehland, <i>et al.</i> [10]	200 kHz	30°
Joseph D. Malone, <i>et al.</i> [11]	400 kHz	40°
Shuabin Ni, <i>et al.</i> [12]	400 kHz	55°
^a ENVISU C2300 OCT	32 kHz	70°

^aNote: ENVISU C2300 OCT (Leica Microsystems GmbH).

from the literatures, as well as commercial devices (labeled with *) in Table 1, ordered by the date of publication. In this Letter, we present a high-speed handheld swept-source OCT system with an unprecedented 105° FOV that extends the imaging area to the peripheral retina based on a non-contact approach. To the best of our knowledge, this is currently the widest FOV for a portable non-contact OCT system.

In this Letter, the novel optical design [Fig. 1(a)] shares the same mechanical parts with the established 400 kHz and 55° FOV handheld OCT/OCTA system [12], except for the telescope design after the slow axis of the galvanometer scanner. The tuning range of the vertical-cavity surface-emitting laser (VCSEL) source is 100 nm, which corresponds to an axial resolution of 4.94 μm in air. The sensitivity of the system was 102.9 dB, and the signal roll-off across the full imaging depth of 6 mm in air was 2.4 dB [Fig. 1(b)]. The scan lens consisted of a paired achromatic doublet lens with a 30-mm-diameter and 80 mm focal length (AC300-080-B, Thorlabs, Inc.). The combination of a 1 in negative achromatic doublets lens with a -100 mm focal

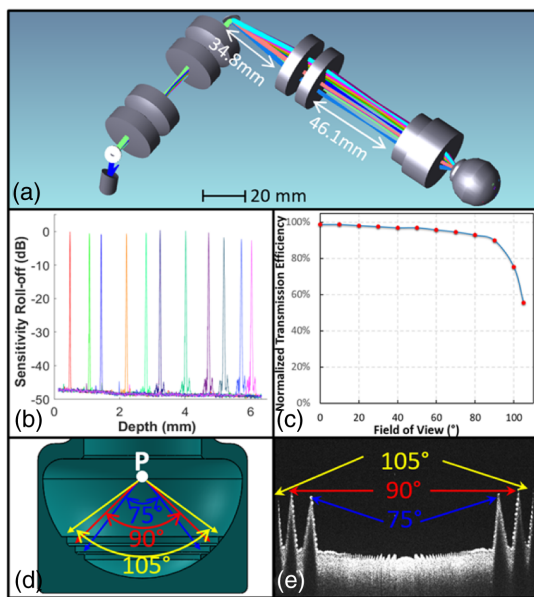


Fig. 1. (a) 3D layout of a handheld UWF OCT probe in OpticStudio. (b) Sensitivity roll-off of 2.4 dB across the full imaging range of 6 mm in air. (c) FOV dependence of measured normalized transmission efficiency. (d) Cross-sectional view of a 3D rendered half-sphere angle target with three concentric ring markers at angles of 75°, 90°, and 105°. (e) Cross-sectional scan of the angle target with the maximum FOV.

length (ACN254-100-B, Thorlabs, Inc.) and an advanced double aspheric lens (Digital Wide Field, Volk Optical, Inc.) was used as the ocular lens. The scan lens and ocular lens worked as a 3.68× telescope, which amplified the scanning angle from 29° out of the scanner to ~105° on the pupil. The working distance from the last lens surface to the cornea was ~5 mm, which is significantly shorter than the previously reported handheld OCT retinal imaging systems. The beam size on the pupil plane was 0.58 mm, resulting in a theoretical focused spot size of 28.1 μm ($1/e^2$ diameter) on the retinal plane when imaging an infant with an axial eye length of 17 mm. The incident power on the cornea was 1.68 mW, which is within the ANSI Z136.1-2014 standards for 1060 nm light.

The advanced double aspheric lens from Volk Optical had 90 diopters of refraction power with a 30 mm diameter, which was commonly used in clinical exams. The lens was made with Volk's patented double aspheric design with minimized peripheral image distortion. Inspired by the characteristic, we sought to further explore the possibility of integrating the lens into our handheld OCT system. The original Volk lens had an anti-reflection (AR) coating for the visible wavelength range which, when used in OCT imaging at 1060 nm, would result in significant attenuation of the incidence power and the reduced collection of backscattered signals from the sample. Custom AR coating (reflectivity <0.5% from 950–1150 nm) was applied to both optical surfaces of the double aspheric lens to improve the transmission in the infrared wavelength range. The incident power at different FOVs was measured to characterize the transmission efficiency of the AR coating, as shown in Fig. 1(c).

A customized 3D printed target [Fig. 1(d)] was used to calibrate the working distance and FOV. This target consisted of three concentric ring markers at angles of 75°, 90°, and 105°. The probe was moved along the axial direction so that the

scanning pivot point is positioned on the center of the sphere, point "P", in Fig. 1(d), and the cross-sectional scan appeared close to flat [Fig. 1(e)]. The cross-sectional scan with the maximum FOV captured all the markers, as seen in Fig. 1(e), which implied that the maximum FOV was ~105°.

The sample arm of the OCT system was simulated and optimized in the OpticStudio (Zemax LLC). The metrics of the spot diagram and the Strehl ratio were used here to evaluate the optical performance of a handheld UWF OCT system. Figure 2 shows the optical performance comparison between our previous design of 55° FOV [12] and the UWF OCT imaging system at the FOV of 0°, 40°, and 55°. The spot diagram and Strehl ratio of the UWF OCT system with the FOV from 60° to 100° are also presented in the last row of Fig. 2(b). The Strehl ratio is shown in the upper left of the Huygens point spread function (PSF) diagram. The spot diagram is commonly used in the evaluation of the OCT system optical performance. The spread of rays and the type of aberrations could be easily observed in the shape of the spot diagram. However, the main problems of this metric were that it could not convey intensity of the spot, and the collected rays did not consider the diffraction-limited response. Unlike the handheld OCT/OCTA system at the FOV of 40° and 55° in which the geometrical aberration dominated compared to the diffraction limit response, the spot diagrams in a UWF OCT system at the FOV of ≤60° were diffraction-limited or near diffraction-limited. Therefore, to evaluate the optical performance of the UWF OCT system more accurately, the Strehl ratio and Huygens PSF with consideration of diffraction were also analyzed here. In the Strehl ratio, the peak intensity of PSF was normalized to unity. In the handheld OCT/OCTA system with a 55° FOV, the optical aberrations would severely degrade the transverse resolution and compromise the image quality when the FOV was larger than 40° as shown in Fig. 2(a). It was difficult to employ adaptive optics into the probe due to the size constraint. For this reason, the OCT imaging system with lower system aberrations at the wide FOV became more desirable. As shown in Fig. 2(b), although we started noticing the aberrations at ≥60°, they were not as severe as the 55° FOV system. The UWF OCT imaging system with a novel optical design proposed in the Letter not only reduced the aberration at the same FOV but also enlarged the FOV remarkably.

Although the bidirectional raster scan has less scanning distortion compared to the unidirectional raster scanning approach [13], it cannot skip scanning the four empty corners in the UWF. To fully utilize the scanner for the UWF, we used a spiral scanning pattern that was first introduced by Oscar *et al.* for intraoperative OCT [14]. The spiral scan at constant linear velocity was performed with 608,400 A-scans (with equal radian and azimuthal spacing at 24.4 μm) per volume in this Letter. Each volume acquisition time was 1.52 s.

OCT images were acquired, processed, and displayed in real time with our graphics processing unit accelerated software OCTViewer [15], which facilitated the alignment process and provided immediate assessment of data quality. The imaging sessions were conducted after the patients were dilated with cyclomydril, and the whole session was completed within 5 min to minimize discomfort for the subjects. Each session started in high-speed alignment mode with a 10 Hz volume rate to locate and align the area of interest (Visualization 1). Once the target area was on the ocular fundus, autofocusing was performed in 1 s

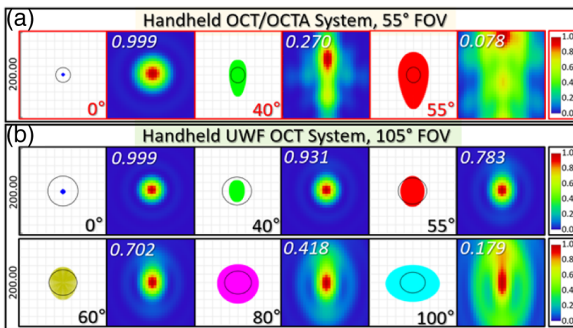


Fig. 2. Spot diagrams and Huygens PSFs from (a) our established system [12] and (b) the UWF OCT system (b) with different FOVs. The scale is 200 μm in the spot diagram for both systems. The radius of the Airy disk (black circle) is 17.06 (55° FOV) and 31.77 μm (105° FOV). The FOV configuration is shown in the bottom right corner of each spot diagram. The Strehl ratio is shown in the upper left of each Huygens PSF.

based on the brightness of the *en face* images with a hill-climbing algorithm [16]. Then we switched to the spiral scan to acquire OCT data. Remapping of the spiral scanning *en face* images was implemented by the nearest-neighbor algorithm in real time and by cubic scattered data interpolation in post-processing (function *griddata* in MATLAB).

In this Letter, three healthy adult volunteers (24–34 years old) and 31 pediatric patients (less than 6 months old) were imaged with the handheld UWF OCT system. All the subjects were recruited from the Casey Eye Institute at the Oregon Health & Science University. The research was approved by the Institutional Review Board/Ethics Committee of OHSU in accordance with the Declaration of Helsinki.

Imaging of the peripheral retina is essential to evaluate the severity of ROP. Peripheral pathology can be difficult, if not impossible, to fully appreciate with standard FOV OCT. Previously, our clinical team has been able to visualize the retinal periphery using scleral depression with our 55° handheld OCT/OCTA system [17], as shown in Figs. 3(a)–3(c), but the ability to acquire imaging of the posterior pole and peripheral retina in a single, continuous scan could greatly improve the diagnosis of retinal diseases [Figs. 3(d)–3(f)]. Using handheld UWF OCT, we screened a similar area of a patient presented with ROP stage 3 by both a bidirectional raster scan (800 A-scans/B-scan, 780 B-scans/volume, total of 624,000 A-scans/Volume) [Fig. 4(a)] and a spiral scan (608,400 A-scans/volume) [Fig. 4(b)]. In the bidirectional raster scan, we noticed the scanning artifacts shown in red arrows in the zoomed-in inset of Fig. 4(a). These scanning artifacts were produced by a sharp change of directions in the fast axis (vertical direction) and hysteresis of the scanners. The distortion was not present when using the spiral scan, seen in the zoomed-in inset of Fig. 4(b). The bidirectional raster scan protocol usually scanned the entire square area; thus, 21.5% of the A-lines allocated in the four corners [white arrows in Fig. 4(a)] would be wasted. In contrast, all A-lines were allocated to the sample using the spiral scan. With the same number of A-lines per volume, the sampling density in the spiral scan is higher than the bidirectional raster scan. Assuming that the infant eye length was 17 mm, the scan region with approximately a 21.5-mm-diameter could be obtained with the 105° FOV. If 608,400 A-lines per volume were implemented in these two scanning protocols,

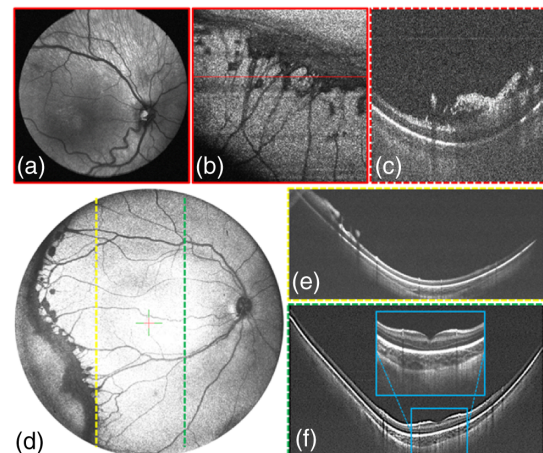


Fig. 3. *En face* OCT images of retina posterior pole from an (a) awake neonate and (b) peripheral retina using scleral depression acquired by a 55° handheld OCT/OCTA system [12]. (c) Selected B-scan [red line in (b)] reveals neovascularization. (d) *En face* OCT image with a clear demarcation line from another infant (ROP, Stage 3) with extra retinal neovascularization acquired by the handheld UWF OCT. (e) Selected B-scan with neovascularization [yellow dashed line in (d)]. (f) Another selected B-scan across the macular region [green dashed line in (d)].

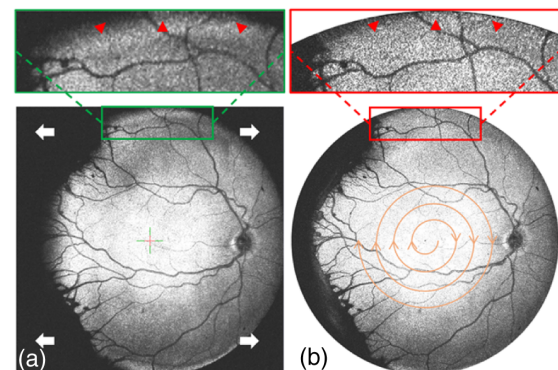


Fig. 4. (a) *En face* OCT image acquired by a bidirectional raster scan. The white arrows denote the four empty corners unavoidable in the bidirectional raster scan. (b) *En face* OCT image acquired by a spiral scan. The zoomed-in insets show the comparison of the edge of the scanning area. Note that the fast scan direction is vertical in the raster scan (a), and the galvanometer scanner turning points are at the top and bottom of the image.

then the scan interval for a spiral scan and raster scan would be 24.4 and 27.5 μm , respectively.

Figure 5 shows a RetCam color fundus image [Fig. 5(a)], fluorescence angiogram image [Fig. 5(b)], *en face* OCT image [Fig. 5(c)], and two represented B-scans [Figs. 5(d) and 5(e)] obtained by our handheld UWF OCT system from a premature infant with ROP after laser treatment. The *en face* OCT image covered an area of the retina comparable to the RetCam fundus image, which is stated to have a 130° FOV. Laser treatment is often effective in reducing neovascularization, but some patients may experience recurrence, resulting in vascular dragging, retinoschisis, and retinal detachment [18], all of which are more easily appreciated on OCT imaging.

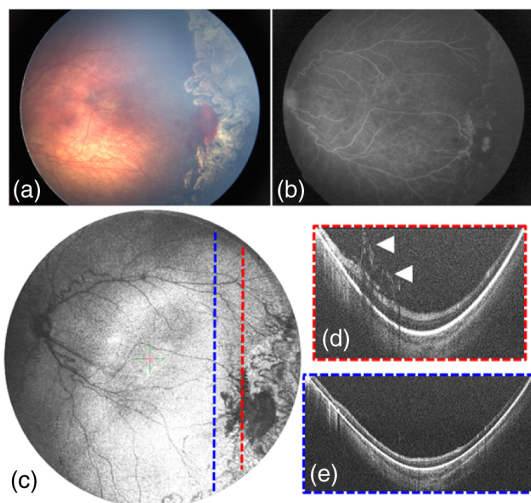


Fig. 5. (a) RetCam color fundus image from an infant with ROP stage 3 after laser treatment. (b) RetCam fluorescein angiogram image. (c) *En face* OCT image acquired by the handheld UWF OCT. (d) Selected B-scan [red dashed line in (c)] reveals neovascularization. (e) Selected B-scan [blue dashed line in (c)] without apparent neovascularization.

The novel optical design of the probe in this Letter significantly improved the optical performance in terms of extending the FOV and controlling the system's aberrations. In the representative *en face* OCT images shown above, there were no pronounced motion artifacts. Although our UWF OCT imaging system was able to acquire a larger area in a single shot compared to our previously published handheld OCT/OCTA system, we did not implement the OCTA scanning pattern in the UWF OCT system due to the constraints of speed and transverse resolution. Resolving capillaries with OCTA require higher sampling density and higher transverse resolution, which are not currently available in our system. Volume acquisition time within 1~2 s is practical in the clinical application. A higher sampling density would lead to a longer volume acquisition time and more severe motion artifacts, which can be mitigated by using a faster swept-source laser. However, the signal-to-noise ratio (SNR) of the OCT signal inevitably decreases with the increasing speed; under the current 1.8-mW laser safety protocol, an OCT system with speed above 1 MHz might only lead to diminishing return [19]. In addition, a larger beam on the pupil will in theory provide better transverse resolution; however, without a better optical design, further increasing the numerical aperture will only lead to larger optical aberrations and possibly lower transverse resolution.

Although the current imaging range of 6 mm in air was sufficient in most cases, careful adjustment was required to avoid aliasing artifacts during scanning. A longer imaging range without appreciable sensitivity roll-off is desired, as it facilitates the alignment process, particularly in the UWF imaging application because of the larger retinal curvature compared to the regular FOV imaging. Moreover, the UWF design further shortens the working distance. With these limitations, the operators have reported that the UWF design is more challenging to align.

Nevertheless, in this Letter, we achieved the widest FOV among all portable retinal OCT imaging research prototypes and commercial systems. Compared to the 100 deg desktop retinal imaging system with an MHz FDML light source [20], our

solution has a significantly higher SNR, longer imaging range and higher quality optics close to the diffraction limit across the entire FOV. The *en face* images presented clearly show the microvascular abnormalities extending from the posterior pole to the peripheral retina in a single capture without pronounced motion artifacts. The spiral scan with real-time visualization was employed here to acquire UWF OCT images. Handheld UWF OCT imaging technology with a non-contact approach and fast acquisition time has the potential to be widely used in the evaluation of pediatric retinal diseases.

Funding. National Institutes of Health (P30 EY010572, R01 EY019474, R01 EY024544, R01 EY027833, R01 HD107494); Research to Prevent Blindness (Career Advancement Award, Career Development Award, Unrestricted departmental funding grant); The West Coast Consortium for Technology and Innovations in Pediatrics.

Acknowledgment. The authors thank Volk Optical, Inc., for providing the Zemax models for the digital wide field lens and the eye, and Dr. Atriya Ghosh for the insightful discussion on the optical design.

Disclosures. Yali Jia: Optovue, Inc. (F, P). David Huang: Optovue, Inc. (F, I, P, R). Other authors declare no conflicts of interest.

Data Availability. Data underlying the results presented in this paper are not publicly available at this time but may be obtained from the authors upon reasonable request.

REFERENCES

- C. Gilbert and A. Foster, Bull. World Health Organ. **79**, 227 (2001).
- W. Jung, J. Kim, M. Jeon, E. J. Chaney, C. N. Stewart, and S. A. Boppart, IEEE Trans. Biomed. Eng. **58**, 741 (2011).
- C. D. Lu, M. F. Kraus, B. Potsaid, J. J. Liu, W. Choi, V. Jayaraman, A. E. Cable, J. Horngger, J. S. Duker, and J. G. Fujimoto, Biomed. Opt. Express **5**, 293 (2014).
- D. Nankivil, G. Waterman, F. LaRocca, B. Keller, A. N. Kuo, and J. A. Izatt, Biomed. Opt. Express **6**, 4516 (2015).
- F. Larocca, D. Nankivil, T. Dubose, C. A. Toth, S. Farsiu, and J. A. Izatt, Nat. Photonics **10**, 580 (2016).
- J. Yang, L. Liu, J. P. Campbell, D. Huang, and G. Liu, Biomed. Opt. Express **8**, 2287 (2017).
- J. P. Campbell, E. Nudelman, J. Yang, O. Tan, R. V. P. Chan, M. F. Chiang, D. Huang, and G. Liu, JAMA Ophthalmol. **135**, 977 (2017).
- O. Nadiarnykh, V. Davidovi, M. G. O. Gräfe, M. Bosscha, A. C. Moll, and J. F. de Boer, Biomed. Opt. Express **10**, 2213 (2019).
- S. Song, K. Zhou, J. J. Xu, Q. Zhang, S. Lyu, and R. Wang, Biomed. Opt. Express **10**, 2383 (2019).
- C. Viehland, X. Chen, D. Tran-Viet, M. Jackson-Atogi, P. Ortiz, G. Waterman, L. Vajzovic, C. A. Toth, and J. A. Izatt, Biomed. Opt. Express **10**, 2623 (2019).
- J. D. Malone, M. T. El-Haddad, S. S. Yerramreddy, I. Oguz, and Y. K. Tao, Neurophotonics **6**, 041102 (2019).
- S. Ni, X. Wei, R. Ng, S. Ostmo, M. F. Chiang, D. Huang, Y. Jia, J. P. Campbell, and Y. Jian, Biomed. Opt. Express **12**, 3553 (2021).
- M. J. Ju, M. Heisler, A. Athwal, M. V. Sarunic, and Y. Jian, Biomed. Opt. Express **9**, 2336 (2018).
- O. M. Carrasco-Zevallos, C. Viehland, B. Keller, R. P. McNabb, A. N. Kuo, and J. A. Izatt, Biomed. Opt. Express **9**, 5052 (2018).
- Y. Jian, K. Wong, and M. V. Sarunic, J. Biomed. Opt. **18**, 026002 (2013).
- A. Camino, R. Ng, J. Huang, Y. Guo, S. Ni, Y. Jia, D. Huang, and Y. Jian, Opt. Lett. **45**, 2612 (2020).
- B. A. Scruggs, S. Ni, T.-T. P. Nguyen, S. Ostmo, M. F. Chiang, Y. Jia, D. Huang, Y. Jian, and J. P. Campbell, medRxiv 2021.10.14.21265026 (2021).
- G. E. Quinn, Arch. Ophthalmol. **123**, 991 (2005).
- Y. Miao, M. Siadati, J. Song, D. Ma, Y. Jian, M. F. Beg, M. V. Sarunic, and M. J. Ju, Opt. Lett. **46**, 3833 (2021).
- J. P. Kolb, T. Klein, C. L. Kufner, W. Wieser, A. S. Neubauer, and R. Huber, Biomed. Opt. Express **6**, 1534 (2015).